Observation of anomalous impurity transport during low-density experiments in W7-X with laser blow-off injections of iron

B. Geiger[1], Th. Wegner[1], C. D. Beidler[1], R. Burhenn[1], B. Buttenschön[1], R. Dux[2], A. Langenberg[1], N. A. Pablant[3], T. Pütterich[2], Y. Turkin[1], T. Windisch[1], V. Winters[5], M. Beurskens[1], C. Biedermann[1], K. J. Brunner[1], G. Cseh[8], H. Damm[1], F. Effenberg[5], G. Fuchert[1], O. Grulke[1], J. H. Harris[7], C. Killer[1], J. Knauer[1], G. Kocsis[8], A. Krämer-Flecken[6], T. Kremeyer[5], M. Krychowiak[1], O. Marchuk[6], D. Nicolai[6], K. Rahbarnia[1], G. Satheeswaran[6], J. Schilling[1], O. Schmitz[5], T. Schröder[1], T. Szepesi[8], H. Thomsen[1], H. Trimino Mora[1], P. Traverso[4], D. Zhang[1] and the W7-X Team‡

[1] Max-Planck-Institute for Plasma Physics, Wendelsteinstrasse 1, Greifswald 17491, Germany
[2] Max-Planck-Institute for Plasma Physics, Boltzmannstrasse 2, Garching 85748, Germany
[3] Princeton Plasma Physics Laboratory, Princeton, New Jersey 08543, USA
[4] Auburn University, Auburn, Alabama 36849, USA
[5] University of Wisconsin-Madison, Madison, Wisconsin 53706, USA
[6] Forschungszentrum Jülich, Jülich 52425, Germany
[7] Oak Ridge National Laboratory, Oak Ridge, Tennessee 37830, USA
[8] Wigner Research Center for Physics, Budapest 1121, Hungary

Abstract. The transport of heavy impurities has been investigated at the Wendelstein 7-X stellarator during core electron root confinement (CERC) experiments. Iron atoms were injected via the laser blow-off technique and analyzed by VUV and X-ray spectrometers. The injected amount of iron does not change the global plasma parameters but yields strong enough line radiation for detailed studies based on the impurity transport code STRAHL. The latter is supplied with neo-classical diffusion and convection profiles from the Drift Kinetic Equation Solver (DKES) and has been embedded into a least-squares fit that searches for additional anomalous diffusion and convection profiles, required to explain the measurements. While the resulting convection velocities agree within uncertainties with neo-classical theory, the anomalous diffusion profile exhibits values more than two orders of magnitude larger than the neo-classical one. This significant level of anomalous transport is possibly explained by turbulence. The high T_e/T_i ratio and flat density profile present during the experiment yield low thresholds for temperature gradient driven modes that are expected off-axis where the obtained diffusion profile peaks.

‡ See the authors list in R. C. Wolf et al., Nucl. Fusion 57, 102020 (2017).

1. INTRODUCTION

Transport studies of heavy impurity ions are an active field in fusion research since the success of future power plants will depend crucially on the radiative cooling from highly charged ions. Highly charged ions maintain bound electrons even at high temperatures, emit intense line radiation and can be used to dissipate the heat from the alpha particles [1]. Since overly strong cooling would extinguish the burning plasma, reliable control of the impurity content and composition is needed. However, sound impurity control might be difficult as the different transport mechanisms, grouped into diffusive and convective contributions with neo-classical or anomalous origin, are not yet completely understood.

In stellarators, the neo-classical transport is particularly strong in plasmas featuring sufficiently low collisionalities, ν^* (defined by the collision frequency of a given particle species, multiplied with its characteristic orbit time [2]). If not interrupted often enough by collisions, electrons and ions that are trapped in magnetic helical ripples experience un-balanced drifts and move radially. The transport arising from these drifts is not intrinsically ambipolar and a radial electric field, E_r, must develop. In case of a stronger drift of electrons than of ions, a positive (outwards-directed) radial electric field appears (electron-root confinement) and in presence of a stronger ion-drift, a negative electric field appears (ion-root confinement). The electric field reduces the radial neo-classical diffusion through an additional and charge-independent poloidal $\vec{E}_r \times \vec{B}$ rotation (with $\vec{B}$ the magnetic field vector). In addition, E_r contributes to the radial convection velocity. The energy gain or loss of a given particle in presence of E_r results in an additional thermodynamic force, which can be found in the drift kinetic expression describing the particle flux, Γ, of a given particle species and charge stage [3]:

$$\Gamma = -\nabla n \cdot D_{11} + n \cdot \underbrace{(D_{11}\, q\, E_r/T - D_{12}\, \nabla\, T/T)} \tag{1}$$

$$\Gamma = -\nabla n \cdot D_{\mathrm{nc}} + n \cdot \qquad\qquad v_{\mathrm{nc}} \tag{2}$$

Here, n and T are a given species' charge stage density and temperature, D_{11} and D_{12} are elements of the neo-classical transport coefficient matrix and ∇ denotes the radial derivative. The second term in equation (1) can be expressed by a convection velocity (v_{nc}) that depends on $q\, E_r$. For highly charged impurity ions this term is particularly strong and points outwards for $E_r > 0$ and inwards for $E_r < 0$.

High-performance plasmas with ion temperatures comparable to the electron temperature feature pure ion-root confinement and are expected to exhibit an inward-directed heavy impurity convection. This could lead to an undesired accumulation of impurities as observed at Wendelstein 7-AS [4] and the large helical device (LHD) [5, 6]. However, recent theoretical findings predict impurity screening in a mixed collisionality regime at high ion temperatures [7]. Moreover, the anomalous impurity transport caused by turbulence might help avoiding accumulation. Turbulent impurity transport can be described by ordinary Fickian diffusion and has no strong mass or charge dependence ($\vec{E} \times \vec{B}$ driven) [8]. In tokamaks enhanced ion temperature gradient (ITG) turbulence is

routinely observed during central electron cyclotron resonance heating (ECRH) [9] and is used as a tool for accumulation avoidance [10]. Also in stellarators, deviations from neo-classical theory, as observed in Wendelstein 7-AS [11] and LHD [12, 13], have been attributed to turbulence. However, clear conclusions were difficult since the uncertainties in modeling the neo-classical transport were large. In the LHD for example, a reduced tendency for impurity accumulation has been observed when applying strong and central ECRH or NBI but it is not clear to which extent this effect is due to a modification of the radial electric field (neo-classical transport) or caused by enhanced anomalous diffusion.

In contrast to most previous experiments, the magnetic field structure of Wendelstein 7-X (W7-X) [14, 15] is optimized for low neo-classical transport. The relative impact of anomalous transport can, therefore, be addressed more easily as presented in this paper. First, the experimental setup and measurements of impurity line emissions will be discussed. Section 3 then provides a description of the modeling tools applied, consisting of DKES [16], used to infer neo-classical diffusion and convection profiles, STRAHL [17], needed for impurity transport simulations and synthetic measurements and KN1D [18], applied to determine neutral background density profiles for STRAHL. In section 4, results from a least-squares fitting routine are presented that allows inferring anomalous diffusion and convection profiles by minimizing the difference between measurements and STRAHL predictions. The impact of measurement- and modeling-uncertainties on the STRAHL results is addressed in section 5 and finally, a discussion and summary are given in sections 6 and 7.

2. EXPERIMENTAL SETUP AND RESULTS

During the 2017 experimental campaign of W7-X, experiments have been performed in the standard magnetic field configuration (labeled EIM [19]) featuring a magnetic field strength of -2.52 T (on axis) and a flat profile of the rotational transform (ι) with values close to unity. Figure 1 shows a top down view of the last closed flux surface of this W7-X configuration, as well as poloidal cross-sections at three different toroidal positions. The effective minor and major radii are a=0.54 m and R=5.53 m, respectively and the plasma volume is about 32 m^3.

For measurement of the main plasma parameters, a comprehensive suite of diagnostics is available. The evolution of the stored energy is monitored by a diamagnetic loop [20] and the line-integrated density is measured by an interferometer diagnostic [21]. Profile information on the electron density and temperature is obtained from a Thomson scattering system [22, 23] with 16 channels and a time resolution of 100 ms. The density profiles are cross-calibrated with the interferometry data since the absolute density calibration of the Thomson diagnostic was lost due to laser misalignment. Information on the ion temperature is provided by the X-ray Imaging Crystal Spectrometer (XICS) [24] via the Doppler broadening of an argon emission line. Since the imaging spectrometer collects line-integrated information from different

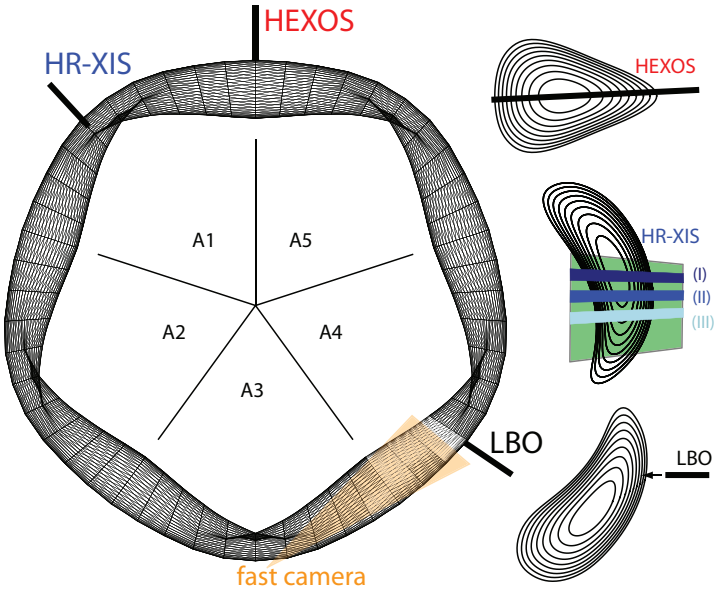

Figure 1. Top down view on the last-closed-flux surface of the W7-X standard magnetic field configuration with poloidal cross-sections at the position of the HR-XIS spectrometer, the HEXOS system and the LBO system. The vertical range covered by the CCD-camera of the HR-XIS system is given in green.

vertical positions, profile reconstruction is required.

Figure 2 shows time traces of a representative experimental program (20171108.020) with hydrogen as main-ion species. The experiment was heated with up to 6 MW of on-axis ECRH power at a line-averaged density of about $2 \times 10^{19}/\mathrm{m}^3$ and featured a plasma stored energy of 350 kJ. The core electron temperature reached up to 6 keV while the central ion temperature is in the range of 2 keV.

Profiles of the electron density for four time points between 0.95 s and 1.25 s are given in figure 3 as a function of the effective radius, r_{eff} normalized to a. The effective radius is defined by $r_{\mathrm{eff}} = \sqrt{\langle A \rangle / \pi}$, with $\langle A \rangle$ the average poloidal flux-surface area. The solid lines in figure 3 shows the result of a spline-fit that will serve as input for the modeling tools described in section 3. The uncertainties indicated by the shaded region have been estimated based on the scattering in the data (with a lower limit of at least 10%) and will be used later to address the sensitivity of the modeling result.

The electron and ion temperature profiles are plotted in figure 4. The electron temperature is significantly higher than the ion temperature, explained by strong on-axis ECRH and the weak thermal coupling between electrons and ions during low density experiments. The spline function used to fit the temperature profiles has been forced to zero at r_{eff}/a=1.2 which explains the shape of the fitted curve in the scrape-off-layer (SOL) region. In addition, it should be noted that such flat temperature profiles in the SOL are even expected due to the presence of magnetic islands in the SOL of W7-X.

At 0.963 s, iron particles were injected into the experiment using a newly installed laser-blow-off (LBO) system [25] that uses the multi-purpose manipulator [26] to position

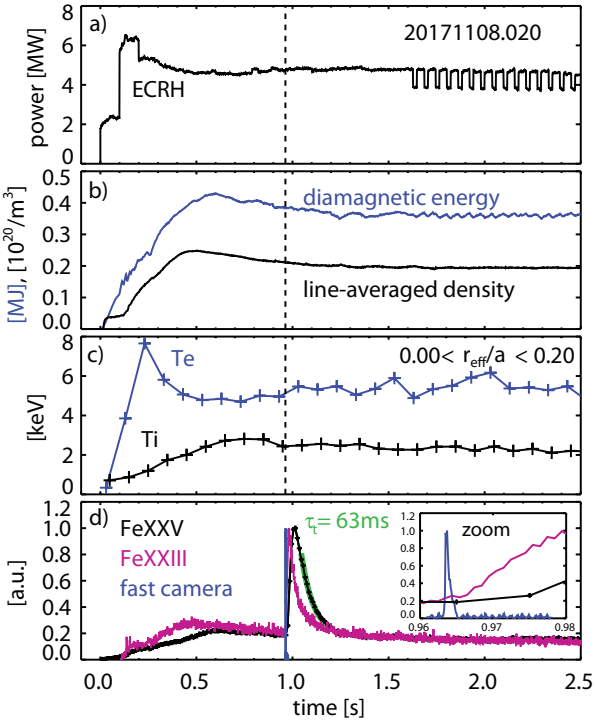

Figure 2. Representative time traces of experimental program 20171108.020, showing the ECRH power (a), the plasma stored energy and line-averaged density (b), the central electron and ion temperatures (c) and normalized emissivities of Fe spectral lines (d) occurring after the LBO injection at 0.963 s. An exponential decay is fitted to the Fe XXV line in (d), which yields an impurity transport time of τ_I=63 ms. From 1.6 s on, one gyrotron of the ECRH system is modulated for heat pulse-propagation studies, not discussed here.

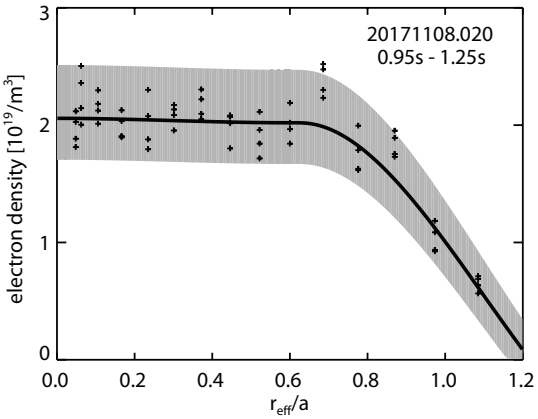

Figure 3. Electron density profile between 0.95 s and 1.25 s as a function of $r_{\rm eff}/a$. The thick lines represent a spline fit to the data. The shaded area indicates the measurement uncertainties.

coated glass targets in the vacuum vessel of W7-X. As illustrated in figure 1, the manipulator with the LBO target holder is located in segment four of W7-X and holds the coated glass targets about 30 cm above the magnetic axis. To ablate and accelerate

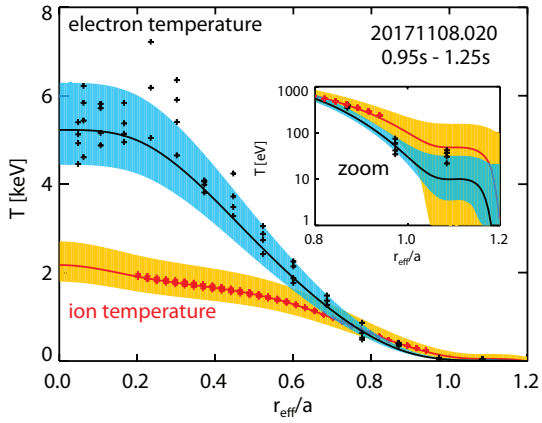

Figure 4. Electron temperature and ion temperature profiles between 0.95 s and 1.25 s as a function of r_{eff}/a. The thick lines represent a spline fit to the data. The shaded areas illustrate the measurement uncertainties.

the coating towards the plasma, a 1 Joule Nd:YAG laser fires onto the backside of the target. The thickness of the coating and the laser spot size on the target define the maximum amount of ablated particles which could theoretically reach the plasma. Here, a thickness of 5 μm and a spot diameter of 4 mm provided a maximum amount of 10^{17} particles.

The LBO injection is clearly visible in figure 2d, showing spectral line intensities measured with two different spectrometers and visible radiation observed by a fast camera. While clear Fe signals are observed after the LBO injection, no effect is seen on the plasma stored energy, density and temperature. This demonstrates that the injected amount of impurities does not perturb the background plasma and permits the assumption of constant diffusion, convection and kinetic profiles during the LBO injection.

The fast camera [27] has an exposure time of 100 μs and monitors the plasma close to the LBO injection (see figure 1). It collects mainly radiation from neutral iron and Fe^{1+} in the visible range where Fe I and Fe II are supposed to radiate (according to the NIST database [28]). The signal from the fast camera (integrated over pixels) is well visible in the zoom of figure 2d and shows that the cloud of ablated particles appears within a time range of about 3 ms.

Higher ionization stages are observed by the High-Efficiency eXtreme ultraviolet Overview Spectrometer (HEXOS) [29, 30] whose line of sight crosses the plasma center in the so called triangular-shaped plane (see figure 1). The HEXOS system consist of four individual spectrometers that cover the spectral range between 2.5 nm and 160 nm and features a time resolution of 1 ms. The temporal evolution of the line radiation following the LBO injection at 0.963 s is shown in figure 5. Spectra in the time range 20 ms before the ablation have been subtracted to show the net effect of the impurity injection. As can be seen, several lines appear after the injection that correspond to different ionization stages, radiating in different regions of the plasma, i.e. at different

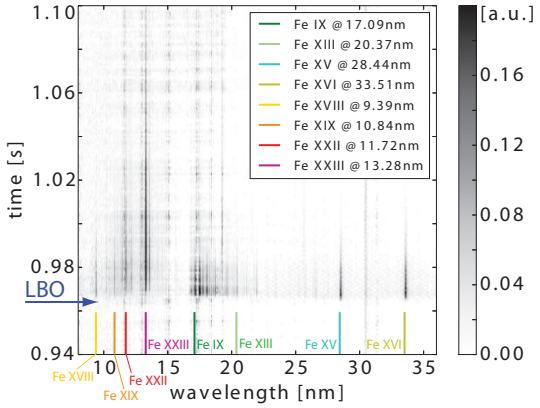

Figure 5. VUV-spectrum (HEXOS) as a function of time from which spectra before the LBO pulse (20 ms) have been subtracted. The color-coded vertical lines highlight the emissions lines, considered here.

temperatures.

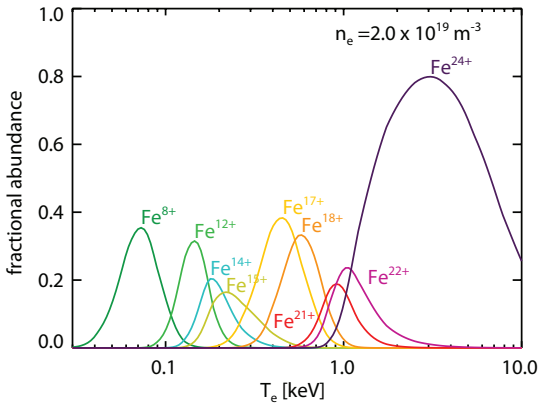

Figure 6. Fractional abundance assuming corona equilibrium (no radial transport) for selected charge stages as a function of the electron temperature.

Figure 6 shows fractional abundances of representative charge stages that are accessible by the HEXOS system (except Fe^{24+}, observed by HR-XIS). While the low charge stages (e.g. Fe^{8+}) are expected at temperatures even below 100 eV, the highest ones appear in the keV range. For the overview-plot in figure 2d, the Fe XXIII emission (Fe^{22+}) has been chosen which is the strongest Fe line in the spectrum and which originates from regions with about 1 keV. Compared to the fast camera data, the peak of the Fe XXIII emission appears with a time-delay since the impurities need some time to move into the hot region of the plasma and to become highly ionized.

The data on the He-like charge stage Fe^{24+}, also plotted in the overview, comes from the High-Resolution X-ray Imaging Spectrometer (HR-XIS) [31, 32]. This spectrometer has a time resolution of 10 ms and monitors the Fe XXV emission at about 0.19 nm. The system utilizes a crystal to disperse the radiation from the plasma and uses a CCD-chip with 195 x 1475 pixels to collect the light. The pixels in the vertical direction correspond

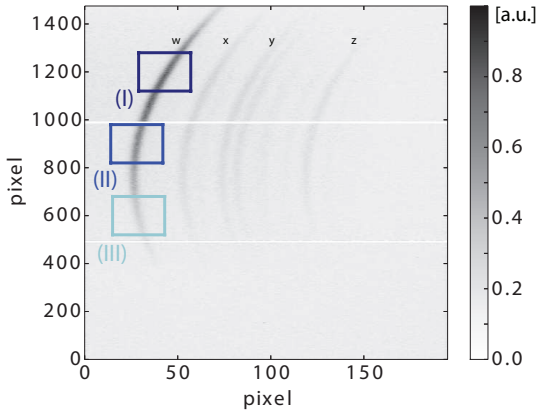

Figure 7. Raw detector image of the HR-XIS diagnostic showing Fe emission lines during experimental program 20171108.020. The boxes illustrate the three regions of interest used to define the lines of sight, displayed in figure 1.

to a fan of 1475 vertical views in the bean-shaped plasma cross-section in segment 1 (see figure 1). The 195 pixels in the horizontal direction collect wavelength information and cover the main Fe XXV excitation lines (w,x,y,z), as well as dielectronic and inner shell excitation satellite lines. As can be seen in figure 7, we define three regions of interest on the CCD-chip which contain the w-line at different vertical positions, labeled (I), (II) and (III). The viewing geometries and widths of these three lines of sight are illustrated in figure 1. It should be noted that there is an un-resolved systematic decrease of the detector signal for pixels above 1300, possibly explained by shadowing effects. The innermost view (I) has, thus, been defined with a slight off-axis geometry.

The time-delay for the peak of the Fe XXV emission in figure 2d is even larger than that of Fe XXIII since Fe^{24+} originates from an even more core-localized region. In contrast to the emission of lower ionization stages, the decay of this emission is not affected by the further ionization into higher stages because the ionization rate of Fe^{24+} into Fe^{25+} is smaller than the back-transition by recombination (assuming 5.8 keV, see figure 11). Thus the transport time, τ_{I} [25], can be inferred from the decay of the Fe XXV line, as shown in figure 2 (τ_{I}=63 ms).

3. MODELING USING DKES, STRAHL AND KN1D

3.1. Drift Kinetic Equation Solver (DKES)

DKES [16] is used to determine profiles of E_{r}, as well as neo-classical diffusion and convection profiles. DKES solves the drift-kinetic equation for closed flux surfaces using a monoenergetic and local ansatz. For a given magnetic field configuration, it returns data-base files with monoenergetic transport coefficients as a function of r_{eff}, ν^* and $E_{\mathrm{r}}/(vB)$ with the particle velocity v and the magnetic field strength B. From the data-base, the neo-classical transport matrix can then be obtained quickly by performing an energy-convolution of the monoenergetic transport coefficients with the appropriate

Maxwell distribution function. The first element of the transport matrix D_{11} is the local diffusion coefficient, D_{nc}, and the local convection velocity, v_{nc}, can be calculated from equation (1), i.e. $v_{\mathrm{nc}} = D_{11}\, q\, E_r/T - D_{12}\, \nabla T/T$. In addition, the transport matrix can be used to compute radial fluxes of electrons and ions and thus allows determination of the E_{r} required to fulfill ambipolarity. Here, an iterative approach has been chosen to find E_{r} values for which the radial flux of electrons and ions becomes equal.

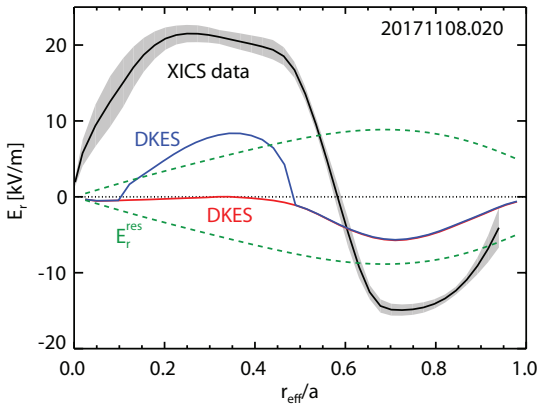

Figure 8. Radial profiles of the electric field resulting from an iterative calculation assuming ambipolarity in DKES. The blue curve shows the result when starting the iteration loop at +20 kV/m and the red curve correspond to -20 kV/m. A reconstructed E_{r} profile from the XICS diagnostic is given in black with the statistical uncertainties indicated in gray. The resonant electric field ($E_{\mathrm{r}}^{\mathrm{res}}$) profile for iron particles is plotted with green dashed lines. $E_{\mathrm{r}}^{\mathrm{res}}$ is defined when the poloidal $\vec{E}_{\mathrm{r}} \times \vec{B}$ precession cancels the poloidal rotation due to particles streaming with thermal velocities along helically twisted field lines.

The fitted kinetic profiles presented in section 2 have been used as input for the DKES analysis. In addition, carbon has been introduced as impurity species with a concentration of 3% of the electron density which refers to an effecive charge (Z_{eff}) of 1.9, being a typical value for fusion experiments [33, 34]. Furthermore, all 26 ionization-stages of iron have been added assuming a negligible concentration, well below the tracer limit. Results of the iterative determination of E_{r} are shown in figure 8. Two solutions are obtained when starting the iteration with either positive (+20 kV/m) or negative (-20 kV/m) values. However, the ion-root solution with negative E_{r} values in the core (red profile) is not supported by data from the XICS diagnostic, additionally shown in black. The data is based on the measured Doppler shift of an argon emission line, providing information on the poloidal plasma rotation and thus on E_{r} when considering the force balance equation [35]. In contrast, the shape of the calculated E_{r} profile in blue is qualitatively consistent with the experimental data. Both profiles are positive in the plasma center (electron-root) and become negative (ion-root) towards the edge. This is expected in presence of strong on-axis ECRH and low densities and is called core-electron-root confinement (CERC [36]). However, the absolute values of the calculated and measured profiles do not agree within the displayed statistical uncertainties, possibly explained by even larger systematic uncertainties in the XICS system calibration (up

to 50%). In addition, ambipolarity would be violated when using the experimenal E_r profile in the DKES analysis such that we choose the calculated E_r profile for further analysis.

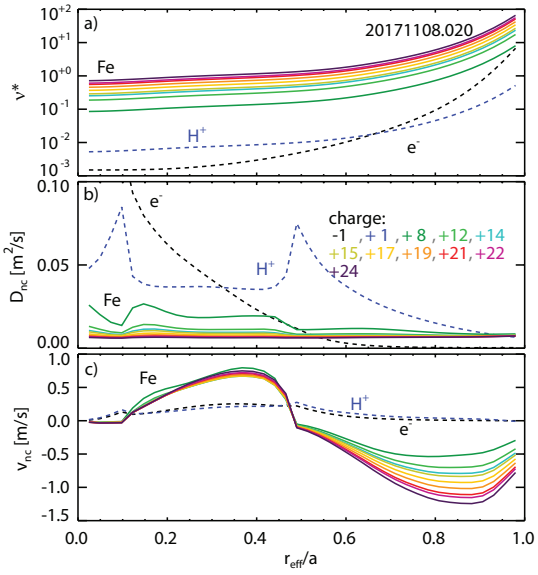

Figure 9. Radial profiles of the collisionality $\nu*$ (a), the neo-classical diffusion (b) and neo-classical convection velocity (c) from DKES for different ionization stages of iron as a function of r_{eff}/a.

The corresponding neo-classical diffusion and convection profiles are displayed in figure 9 for electrons, main-ions and different charge stages of iron. The strength of the neo-classical diffusion scales inversely with charge (q) since the curvature and gradient B drifts, dominating neo-classical transport, depend on $1/q$. This can e.g. be seen by a stronger diffusion of main-ions than of the iron particles. The peaks of the main-ion diffusivity at r_{eff}/a=0.1 and r_{eff}/a=0.5 are localized where E_r crosses zero (see figure 8) and can be explained by the absence of the $\vec{E}_r \times \vec{B}$ induced poloidal rotation which is needed to reduce the neo-classical diffusion. For the impurities, however, we observe the opposite behavior, meaning that D_{nc} increases with E_r. This effect can be explained since the E_r profile is close to $E_r^{\mathrm{res}} = \iota v_{\mathrm{th}} B r_{\mathrm{eff}}/R$ [37] with the thermal velocity of iron v_{th}. The resonant electric field is defined by the condition that the $\vec{E}_r \times \vec{B}$ poloidal precession cancels the poloidal rotation due to particles streaming along helically twisted field lines. When E_r is close to E_r^{res} for a given particle species, particle trajectories can exist that do not rotate poloidally on the flux surface such that drifts are not balanced any longer, yielding strong neo-classical diffusion. Finally, it should be noted that the obtained neo-classical diffusivities are still very small, which is a consequence of the optimization of W7-X with respect to neo-classical transport.

Figure 9c shows neo-classical convection velocity profiles, v_{nc}, for different charge stages. The strength of the v_{nc} profile scales with charge and it's shape is closely related to the E_r profile since the first term in equation 1 dominates for highly charged ions. From center to the edge, the convection velocity of iron particles drives impurities

outwards and then becomes inward-directed. The small absolute values of the neoclassical convection velocity (below 1.5 m/s) are explained by the dependence of v_{nc} on D_{11}.

3.2. KN1D

The KN1D code [18] has been applied to calculate neutral background densities which can affect the charge stage distribution of Fe via charge-exchange collisions. KN1D is a 1D code that calculates the H_2 gas flux from the wall, the dissociation of H_2 molecules and finally the propagation of H into the plasma considering ionization and charge-exchange reactions. Here, KN1D is supplied with the same kinetic profiles as used in DKES. Additionally, KN1D would require the hydrogen gas density and temperature (pressure) close to the wall. Since this information is not available, we consider an arbitrary density ($1 \times 10^{17}\,\mathrm{m}^{-3}$) and wall temperature (3 eV) and scale the resulting profiles to the edge-neutral density measured from filterscopes [38]. The latter observe a flux of H-atoms between 10^{18} and 10^{21} particles per second and m^2, depending on the 3D measurement location. The measured fluxes can be translated into neutral densities by considering an edge neutral temperature of 3 eV (the Franck-Condon dissociation energy of H_2), i.e. a velocity of 24 km/s for hydrogen. Figure 10 shows resulting neutral density profiles from KN1D in gray dashed lines which have been scaled to an edge density of 4×10^{13} and $4\times10^{16}\,\mathrm{m}^{-3}$ (according to the measured fluxes of 10^{18}-10^{21}/s/m^2). The impact of the high and low density will be discussed in section 5. For the modeling results discussed in section 4, the intermediate density profile (black) will be considered.

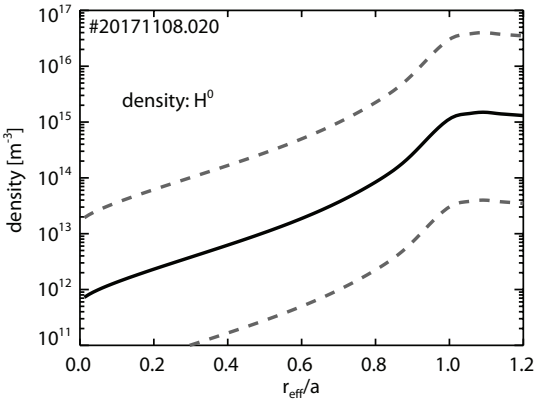

Figure 10. Neutral density profiles of H from KN1D as a function of r_{eff}/a. The dashed lines represent the uncertainties, considered during the sensitivity study presented in section 5.

3.3. STRAHL

The STRAHL code [17] is applied to calculate emissivity profiles of selected spectral lines. STRAHL solves the impurity transport equation as a function of the impurity

charge stage and effective radius (1D calculation) and requires kinetic profiles (optionally also the neutral density profiles), the device geometry, time traces of the impurity source and atomic data. Moreover, a parameter file is needed that contains e.g. settings for the impurity source location, the time-steps of the simulation or information on the plasma species. One can also specify anomalous diffusion and convection profiles while the neo-classical profiles are typically calculated within STRAHL by a built-in and tokamak-specific neo-classical module (NEOART). For W7-X, we added the possibility to consider the charge-dependent D_{nc} and v_{nc} profiles from DKES, similar to the approach described in [39].

The kinetic profiles input to STRAHL are the spline functions, already discussed in section 2. As radial coordinate for those profiles in STRAHL, the normalized volume, ρ_{vol} is used:

$$\rho_{\mathrm{vol}} = \sqrt{\frac{V}{2\pi^2 R}} \tag{3}$$

Here, V is the volume enclosed by a given flux surface. The ρ_{vol} coordinate permits an accurate description of the radial impurity fluxes and can be directly compared with (is actually equal to) the r_{eff} coordinate on which the W7-X data is mapped.

The distance between the last closed flux surface and the plasma-vessel (wall) has been set to 10 cm in the simulation. This implies that the maximum r_{eff}/a value considered in STRAHL is about 1.2. When modeling the flux of particles in the SOL, STRAHL considers a connection length, L_c, and parallel flow velocity into the divertor. The flow velocity is set to a mach-number of 0.2, while L_c=250 m is used according to [40]. The impact of the choice of L_c and the mach-number will be discussed in section 5. The divertor and the first wall define two sinks of particles in the simulation from which recycling has been turned off since Fe does not recycle.

The position of the LBO source in STRAHL is at the actual target positions (63 cm distance to the last closed flux surface) from which Fe atoms are launched with an energy of 20 eV, as inferred from a time of flight analysis of fast camera data. Data from the fast camera is also considered to describe the temporal shape of the impurity source (see figure 2) while the total number of particles has been set to 10^{17}, as estimated in section 2 as an upper limit. The start of the LBO injection in STRAHL is defined 1.5 ms prior to the rise of the observed Fe IX emission. This is coarse but cannot be improved further since the timing of the laser and the time-base of the fast camera (seeing the Fe emission in the visible spectral range) are even worse. The impact of this timing uncertainty on the modeling result will be discussed in section 5. It should be noted that the time-bases of the HEXOS and HR-XIS systems are accurate to 1 ms.

The transport equations for a given ionization stage are coupled via the ionization, recombination and charge exchange rates into and from neighboring stages. Here we use existing temperature- and density-dependent database files from ADAS [41], labeled scd89_fe for ionization, acd85_fe for recombination and ccd89_fe for charge exchange. An example of the applied recombination and ionization rates is plotted in figure 11. Moreover, photo-emission coefficient 'PEC-files' (as a function of density and

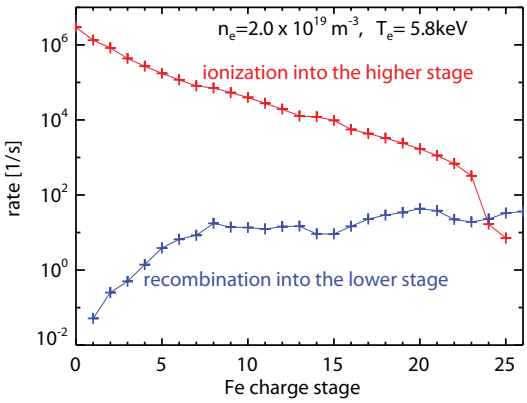

Figure 11. Ionization and recombination rates used in STRAHL as a function of the charge stage, assuming an electron temperature of 5.8 keV and an electron density of $2 \times 10^{19}/m^3$.

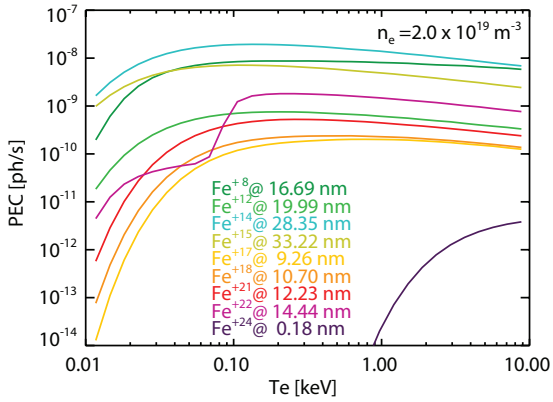

Figure 12. Photo emission coefficients considered by STRAHL as a function of the electron temperature, assuming an electron density of $2 \times 10^{19}/\mathrm{m}^3$.

temperature) are required for the calculation of specific line emissions. The latter have recently been calculated using a modern set of ADAS codes [42] and are illustrated in figure 12 for selected spectral lines. The PEC values depend only weakly on the electron density and do not strongly change at electron temperatures above 100 eV (except for the Fe XXV line).

The output of STRAHL contains radial emissivity profiles as a function of time. These profiles need to be line-integrated per time-step before a comparison with the experimental data is possible. For the line-integration, r_{eff}/a values along the path of a given line of sight have been determined using VMEC [43] equilibrium calculations and extrapolation into the SOL. Figure 13 illustrates radial profiles of those r_{eff}/a values for the HEXOS and HR-XIS views. The HEXOS view has a longer path through the plasma than the HR-XIS views since it crosses the triangular shaped plane and not the slim bean-shaped plane. In addition, the HEXOS view reaches the plasma center ($r_{\mathrm{eff}}/a \approx 0$) while the HR-XIS views exhibit a more or less pronounced off-axis character.

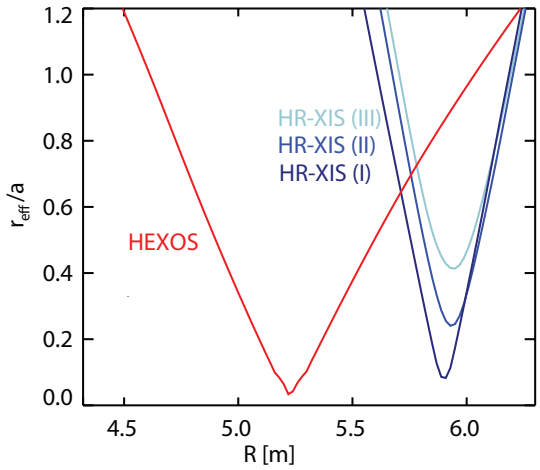

Figure 13. Normalized effective radius, r_{eff}/a, present along the lines of sight of the HEXOS and HR-XIS spectrometers as a function of the major radius.

4. MODELING RESULTS

A set of nine representative emission lines from the HEXOS and HR-XIS spectrometers has been chosen for the detailed impurity transport analysis. Their evolution is plotted in figure 14 together with forward modeling results. The data from the HEXOS system has been normalized individually since a reliable calibration is not yet available. The three emissivities from the HR-XIS diagnostic have been normalized relative to the central line of sight (I), since also here, an absolute calibration was not available.

As a first step, the D_{nc} and v_{nc} profiles from DKES were input to STRAHL in order to check whether the assumption of pure neo-classical transport can already explain the data. An additional ad-hoc anomalous diffusion of $0.1\,\mathrm{m}^2/\mathrm{s}$ was added in the SOL where D_{nc} and v_{nc} are not defined such that the injected Fe-ions can reach the confined region.

The simulation result is shown by the black, dashed lines in figure 14. It clearly disagrees with the experimental data. Very long time-delays are predicted for the radiation from the higher charge stages which are not seen experimentally. For the Fe XXV emission, the time-delay is even too large for the chosen time window such that one cannot see the peak of the emission curve. This demonstrates that additional anomalous transport is present moving the injected particles into the plasma center much quicker than expected from neo-classical theory.

To obtain more details on this anomalous transport, least-squares fitting is applied similar to the approaches described in [44, 45, 46]. The fitting algorithm modifies additional anomalous D_{a} and v_{a} profiles in STRAHL and searches for parameters that minimize the sum of squared residuals, $\mathcal{X}^2$:

$$\mathcal{X}^2 = \sum_i \left(\frac{I[i] - S[i]}{\sigma[i]} \right)^2 \tag{4}$$

Here the sum goes over i data points $I[i]$, $S[i]$ is the model function (STRAHL) and $\sigma[i]$ are the measurement uncertainties. The latter are considered to be the square root

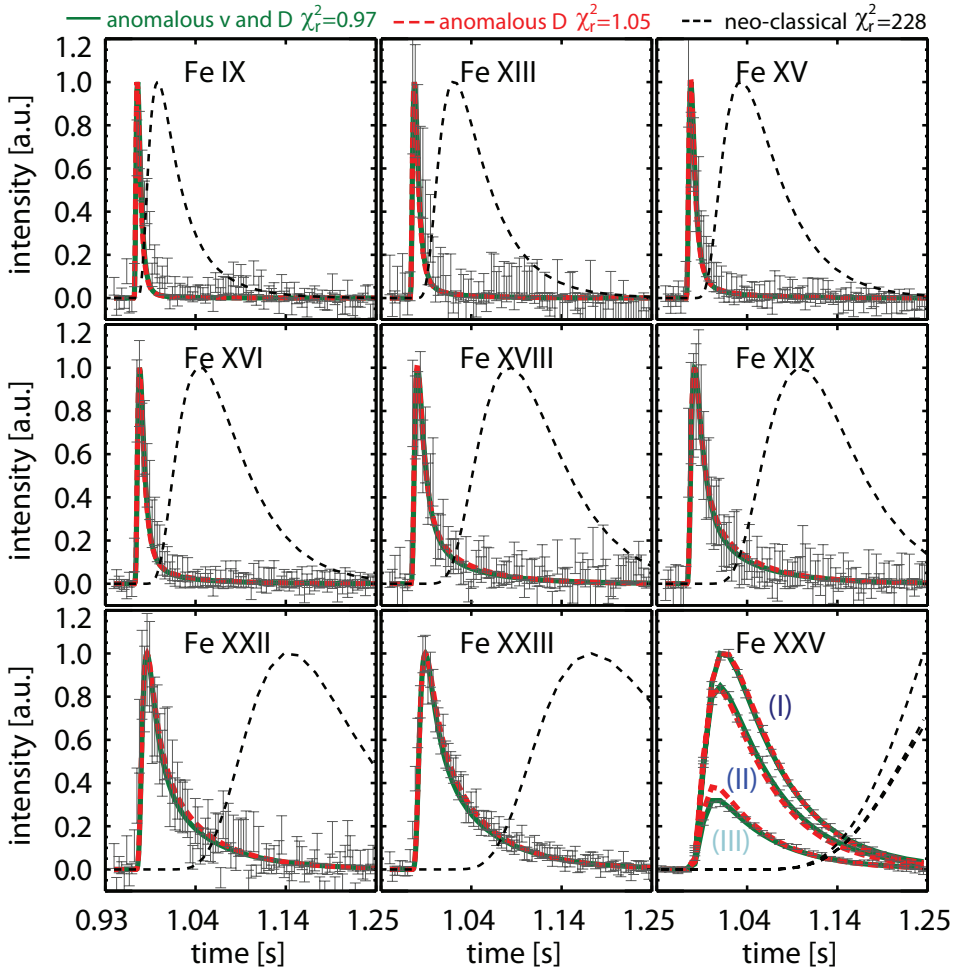

Figure 14. Time traces of nine different emission lines observed by the HEXOS and HR-XIS spectrometers. The results of a STRAHL simulation based on neo-classical $D_{\rm nc}$ and $v_{\rm nc}$ profiles are given by the black, dashed lines. The simulation in red (dashed) shows the result when fitting the data by an additional $D_{\rm a}$ profile (plus some SOL convection) and the green curves correspond to a fit of the data with additional anomalous $D_{\rm a}$ and $v_{\rm a}$ profiles.

of the measurement values before normalization (photon statistics) plus an estimate for the readout noise. In addition, the data of the HR-XIS signal has been weighted by a factor of $\sqrt{30}$ since 30 times more data points are available from the HEXOS system. The temporal resolution of HEXOS is 10-times higher (1 ms instead of 10 ms) and three times more spectral lines/views are used. Without this extra-weighting, the few HR-XIS data points would not be considered sufficiently by the fit.

First we test the hypothesis of additional anomalous diffusion in combination with pure neo-classical convection velocities (except the for SOL). The $D_{\rm a}$ profile to be modified in STRAHL is parametrized with four spline-knots at $r_{\rm eff}/a$=[0.1, 0.4, 0.8, 1.1] and outside the knots at $r_{\rm eff}/a$=0.1 and $r_{\rm eff}/a$=1.1, the $D_{\rm a}$ profile is continued flat. The position of the innermost spline-knot has been chosen at $r_{\rm eff}/a$=0.1 since information

on the plasma core is limited. The slight off-axis geometry of the innermost HR-XIS view and the absence of lower ionization stages in the hot core (no HEXOS data) make conclusions for this region difficult. The innermost knot-value is constrained between $0\,\mathrm{m}^2/\mathrm{s}$ and $0.3\,\mathrm{m}^2/\mathrm{s}$ to avoid unphysical results while the other knot values might be changed by the fit between $0\,\mathrm{m}^2/\mathrm{s}$ and $4\,\mathrm{m}^2/\mathrm{s}$. The v_a profile is set to zero in the confined region and in the SOL it is defined by one value (at r_eff/a=1.1) that might be varied between -3 m/s and +3 m/s.

During the fitting process, an initial fit-run is performed with free knot-values and fixed knot-positions. Then, a second fit-run is performed with the result of the first fit-run as initial guess and with the additional freedom to change the position of the inner two spline-knots of the D_a profile between r_eff/a=0.15 and r_eff/a=1.05.

The evolution of spectral emissivities from the fit-result are plotted in figure 14 with red, dashed lines. The synthetic data agrees well with the measurements, also indicated by a reduced $\mathcal{X}^2$ value of 1.05 ($\mathcal{X}^2_r = \mathcal{X}^2/N$, with N the number of measurement points). The time-delay, rise-time and decay of all charge stages are recovered well by the fit.

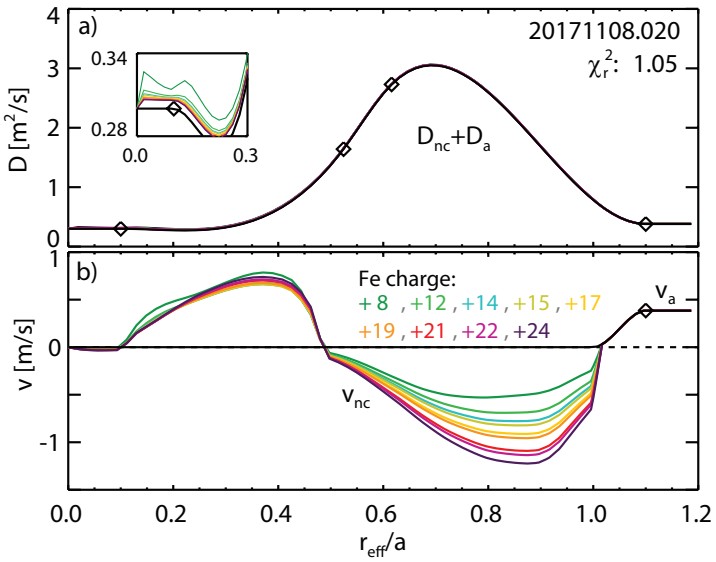

Figure 15. Diffusion and convection profiles obtained when fitting the data in figure 14 with D_a and assuming $v_\mathrm{a} = 0$ in the confined region. In black are given the considered anomalous profiles with the spline-knot positions illustrated by squares.

The corresponding $D = D_\mathrm{nc} + D_\mathrm{a}$ profile is plotted in figure 15a, together with the spline-knots of the D_a profile, indicated by the squares. The D_a profile is more than two orders of magnitude larger than the neo-classical expectation such that the charge-dependent neo-classical contribution is hardly visible and a zoom is needed. Figure 15b shows for selected charge stages the $v = v_\mathrm{nc} + v_\mathrm{a}$ profiles considered by the fit. As discussed before, v_a is zero in the confined region. For the SOL, the fit finds positive convection velocities of about 0.5 m/s that might be explained by the positive electric field, present in the SOL due to the fast parallel flux of electrons into the divertor region, leaving the positively charged ions behind.

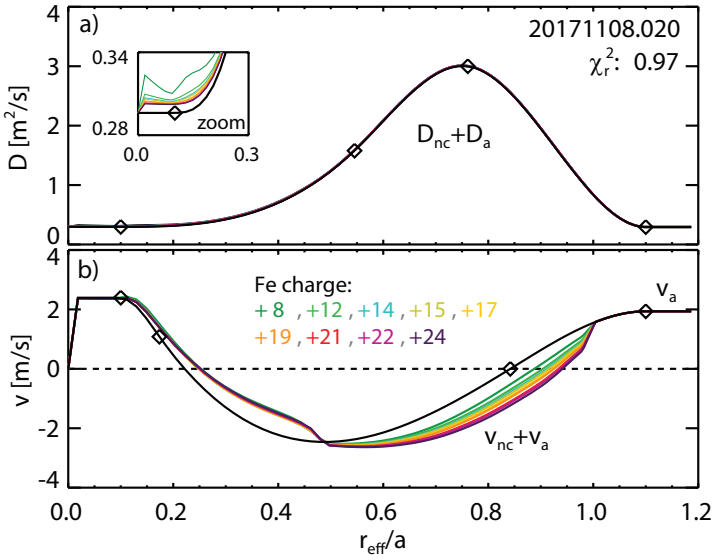

Figure 16. Diffusion and convection profiles obtained when fitting the data in figure 14 with D_a and v_a profiles. In black are given the considered anomalous profiles with the spline-knot positions illustrated by squares.

To address the possibility of additional anomalous convection velocities, a third fit run has been performed with the v_a profile described by four spline points, similar to the D_a profile. As initial guess, the previous result has been applied and, again, the fit is performed within two steps. First, only knot values of D_a and v_a are modified. Then, the inner two spline-knot positions of the D_a and v_a profiles can be additionally varied.

Figure 16 displays the D and v profiles corresponding to this fit-result. The D_nc+D_a profile is close to the previous case and the shape of the $v_\mathrm{nc} + v_\mathrm{a}$ profile resembles the neo-classical prediction. However, the absolute level of the anomalous convection profile, additionally plotted with thin black lines, is about twice as large as v_nc.

The emissivities as a function of time from this fit are displayed in green in figure 14. As indicated by a reduced $\mathcal{X}^2$ value of 0.97, a slightly better representation of the measurements is found. In particular the evolution of view (III) of the HR-XIS system does now agree almost perfectly.

To discuss this fit-result in more detail, figure 17 shows reconstructed Fe density profiles for various time-points on a semi-logarithmic scale. Shortly after the LBO pulse, the Fe density is peaked at r_eff/a=1.15 where the incoming Fe neutrals get ionized. Then, the Fe cloud moves inwards and reaches the plasma center after about 20 ms. During this first phase, strong radial gradients appear such that diffusion can dominate the impurity flux and short time-delays are obtained. Theoretically, also strong and inward-directed convection velocities could explain the fast-inwards movement of Fe. This would, however, mean that impurities are well confined in the plasma and would contradict the observation of τ_I=63 ms. The transport time corresponds to the longest eigentime of the transport equation and is typically set by the lowest diffusivity (and or lowest v values (negative ones)) in the profile. The combined analysis of τ_I and the

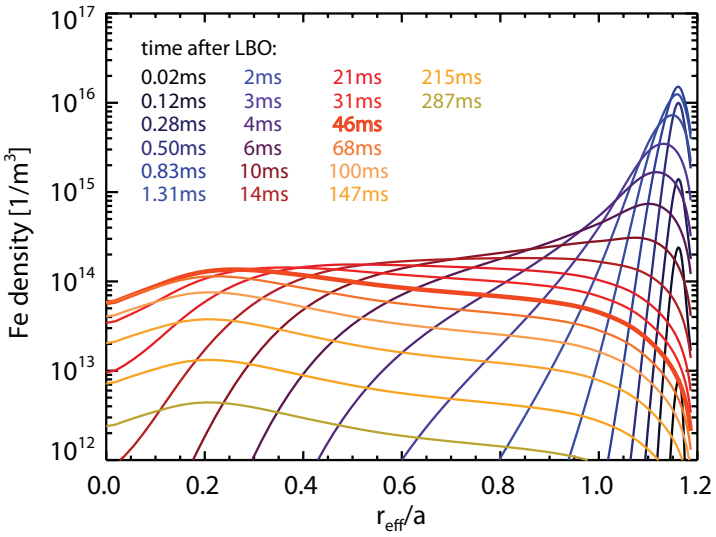

Figure 17. Radial Fe density profiles from STRAHL for different time-points.

time-delay thus allows us to conclude without ambiguity that the anomalous transport is dominated by diffusion and that, if present, only small anomalous convection velocities ($< 5\,\mathrm{m/s}$) can be present.

The second phase after the inward-movement of the density front is characterized by a constant logarithmic profile shape $\nabla log(n) = \frac{\nabla n}{n}$. At times, t, that are longer or comparable with τ_I, the impurity density decays with $n \sim n_0(r)\, e^{-\frac{t}{\tau_\mathrm{I}}}$ at all radii, r such that $\frac{\nabla n}{n}$ is constant in time. This explains well the simulation in figure 17 where all profiles for $t > 46\,\mathrm{ms}$ exhibit the same density peaking. The density peaking is closely related to the v/D profile, which can be understood when rearranging equation (2):

$$\frac{\nabla n}{n} = v/D - \frac{\Gamma}{n\,D} \tag{5}$$

In case of equilibrium conditions ($\Gamma = 0$, not present here) or large D values, the second term on the right hand side of equation 5 vanishes or becomes small, showing the close relation between $\frac{\nabla n}{n}$ and v/D.

Experimentally, the $\frac{\nabla n}{n}$ is accessed by the Fe XXV emission, probed at three different positions. Figure 18 shows in black the modeled Fe XXV emission profile, together with vertical dashed lines for the minimum r_eff/a positions, reached by the three views of the HR-XIS system. The fit of D_a and v_a finds positive v/D values (see figure 16) in the center to obtain a hollow Fe XXV emission profile because view (I) exhibits only slightly stronger signals than view (II) (see figure 14) despite its longer path through the plasma (see figure 13). To additionally reproduce the weak Fe XXV signal from view (III), the third fit concludes with negative v/D values outside r_eff/a=0.2, yielding a negative Fe density peaking. This translates to a Fe XXV emission profile which decreases for r_eff/a >0.2. In contrast, the fit assuming pure neo-classical convection velocities cannot reproduce the peaking of the Fe XXV emission well since v_nc is positive between r_eff/a=0.1 and r_eff/a=0.5. Thus, the evolution of view (III) in

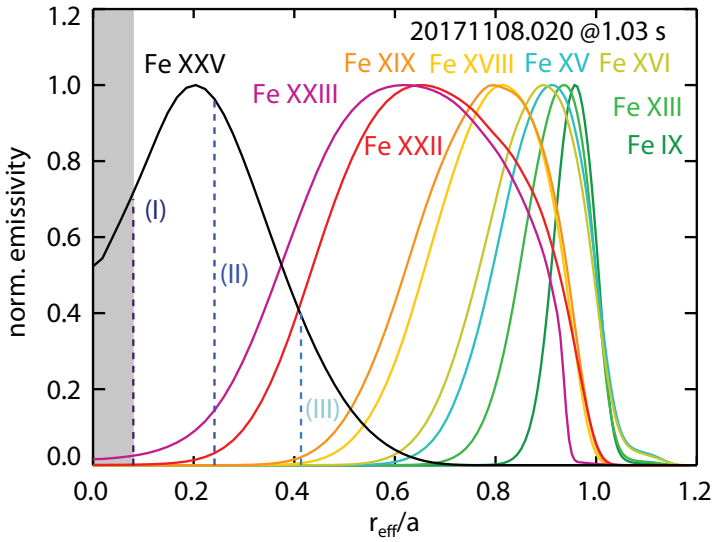

Figure 18. Radial emissivity profiles from STRAHL (normalized) as a function of $r_{\rm eff}/a$.

figure 14 is not perfectly matched by the red curve.

This shows that the Fe XXV emission profile yields valuable information on v/D for $r_{\rm eff}/a$ <0.6. Outside this region, radiation from Fe XXV is not expected because the PEC coefficient of the Fe XXV emission becomes relevant only above about 1 keV (see figure 12).

However, the reconstructed $v_{\rm a}$ profile appears to be very sensitive to the observed peaking of the Fe XXV radiation profile. The small difference between the synthetic emissivities in figure 14 (compare the green and red curves) correspond to a change of the $v_{\rm a}$ profile by about a factor of two. Given the systematic uncertainties of the HR-XIS diagnostic and the modeling, this makes a clear conclusion on the presence of anomalous convection velocities very difficult.

Finally, it should be noted that the fit-result presented here justifies that we are ignoring the effect of the injected impurities on transport. Inside the confined region, the impurity density is well below $10^{15}/\mathrm{m}^3$ for all time-points. This is more than four orders of magnitude lower than the electron density and is low enough to be below the tracer-limit [47]: $n_Z\,Z^2 \ll n_e$, where Z is the impurity charge, n_Z the impurity density and n_e the electron density. Also in the SOL region, where the n_Z is higher (about $10^{16}/\mathrm{m}^3$) and n_e lower, the tracer-limit approximation is still fulfilled since only low charge stages appear, such that $n_Z\,Z^2/n_e$ remains below 0.05.

5. SENSITIVITY STUDY

The uncertainty of the profile reconstruction motivates a sensitivity study by varying the input parameters and profiles in DKES and STRAHL. 14 additional fit-runs were performed during which one given input profile or input setting has been modified. The

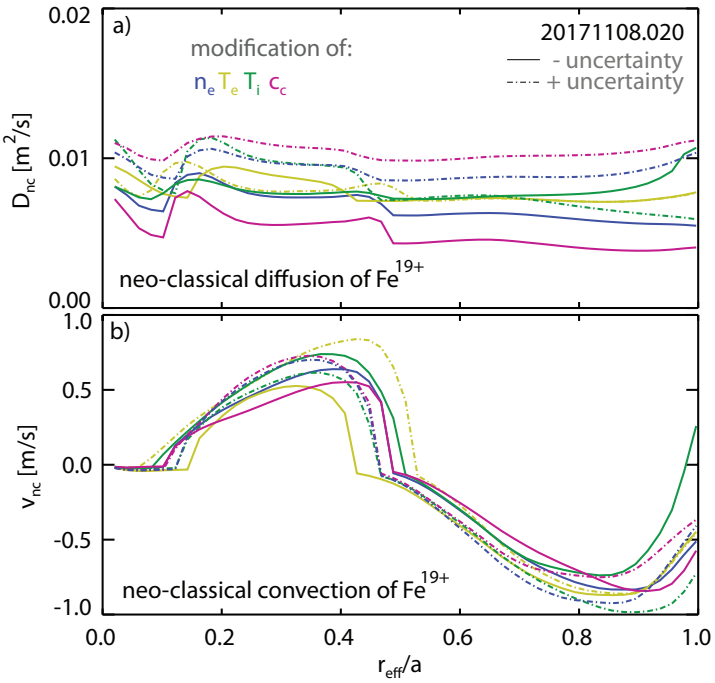

Figure 19. Radial profiles of $D_{\rm nc}$ (a) and $v_{\rm nc}$ (b) from DKES obtained when varying the input profiles. The solid lines represent reduced values in the input profiles. The dashed lines represent increased values in the input profiles.

kinetic profiles (n_e, T_e and T_i) have been varied in DKES according to the upper and lower uncertainty boundaries plotted in figures 3 and 4. In addition, the carbon density (c_c) was modified in DKES to be either 1% or 5%. New $E_{\rm r}$ profiles have been calculated for each case yielding, together with the modified kinetic profiles, different values for $D_{\rm nc}$ and $v_{\rm nc}$. The resulting $D_{\rm nc}$ and $v_{\rm nc}$ profiles are displayed in figure 19 for the intermediate charge stage Fe^{19+}. The solid lines correspond to reduced values in the kinetic profiles (and c_c) and the dashed ones represent increased values. The individual parameters which have been modified are described by the color-code.

Variations of up to 50% of the neo-classical diffusion are observed when e.g. modifying the carbon concentration. However, the overall level remains small and negligible compared with the anomalous transport, required to explain the measurements. The strongest effect on the $v_{\rm nc}$ profile comes from the variation of the electron temperature, well explained due to its strong impact on the radial electric field. When e.g. increasing the electron temperature (dashed light-green lines), the electron-root character of $E_{\rm r}$ is amplified, yielding larger convection values.

For each modified parameter or profile the fitting method, described in section 4 has been used with for spline-knots for $D_{\rm a}$ and the assumption of pure neo-classical convection velocities. The resulting $D_{\rm a}$ profiles are displayed in figure 20. Again, the solid lines correspond to reduced values and the dashed ones represent increased values. The fit quality is indicated by the color-coded $\mathcal{X}_r^2$. As can be seen, changing the electron density, ion temperature or carbon concentration does not strongly change the results.

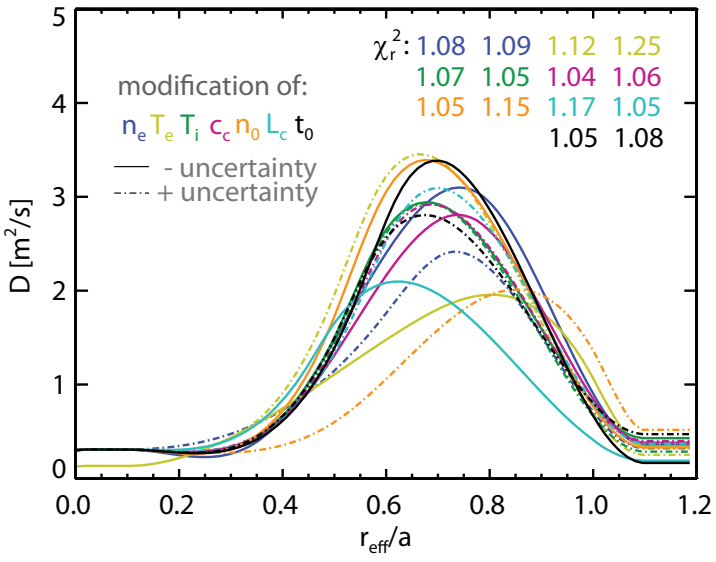

Figure 20. Anomalous D_a profile obtained when modifying the input profiles and settings. The modified settings and profiles (reduced and increased ones) and the resulting $\mathcal{X}_r^2$ values are color-coded. The first $\mathcal{X}^2$ value of a given setting/profile corresponds to reduced settings/profiles (solid lines) while the second one corresponds to increased settings/profiles (dashed lines).

Instead, modifying the electron temperature profile has a larger impact on the fit-results since it affects the ionization location of the injected Fe atoms, the fractional abundance and PEC-coefficients in STRAHL. Both, reduced and increased electron temperature profiles result in a reduced fit-quality ($\mathcal{X}_r^2 > 1.10$).

The impact of changing the neutral density profile, n_0, according to the boundaries plotted in figure 10, is displayed in orange in figure 20. Lowering the neutral density has no impact on the fit quality while increasing the neutral density yields $\mathcal{X}_r^2$=1.15 due to overly strong charge-exchange losses of the Fe^{24+} stage.

For the fit-result plotted in light-blue, the connection length, L_c, has been set to 50 m (solid lines) and 10^6 m (dashed lines). This changes the loss time of particles into the divertor, $\tau_{div} = L_c/v_{flow}$ where v_{flow} is the flow velocity. To match the experimental transport time when L_c (τ_{div}) is low (solid line), the fit reduces the D_a values in the SOL. In contrast, it balances enhanced connection lengths by a higher SOL-diffusion (dashed line). Changing the D_a values in the SOL does, however, affect the modeled time-delay such that the fit quality degrades. It should be noted that changing v_{flow} has a very similar effect (it is also related to τ_{div}) such that a separate discussion is superfluous.

Finally, the timing of the LBO pulse, t_0, has been modified by ±1 ms. The resulting anomalous D_a profiles are plotted in black in figure 20. The reduction of the LBO start-time in STRAHL (-1 ms) yields a lower diffusion profile in the SOL because a slower radial movement of the ablated Fe cloud is required to reach the emission layer of the Fe IX line in time. In contrast, increasing the start-time by +1 ms yields a higher

diffusion value in the SOL.

In summary, a good representation of the spectrometer data is possible with v_a=0 even when modifying the input profiles or settings in STRAHL. The modification causes only small variations in the resulting D_a profiles, which indicates that the D_a profile is well constrained.

6. DISCUSSION

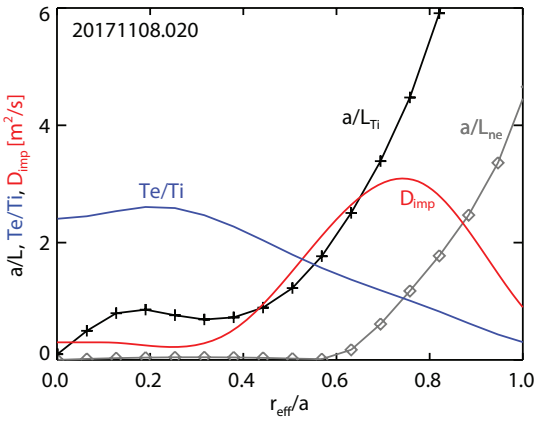

Figure 21. Normalized gradient length profiles of the ion temperature (back crosses) and the electron density (gray squares) compared with the T_e/T_i ratio (blue) and the anomalous diffusion obtained when fitting the data with v_a=0.

The optimization of W7-X with respect to the neo-classical transport makes it easy to demonstrate the presence of anomalous impurity diffusion. The D_{11} transport coefficient is small and not only results in small D_{nc} values but also in reduced v_{nc} profiles (see equation (1)). This situation is similar to tokamaks where radial transport is typically dominated by turbulence. In W7-X, turbulence has already been identified to affect the energy confinement time [48] which can be significantly smaller than expected from neo-classical theory. Also during the experiment discussed here, the energy confinement time, τ_E, is only 80 ms (estimated from the ratio of the plasma stored energy (0.4 MJ) and the applied heating power (5 MW) during steady state), which is much smaller than predicted by neo-classical transport modeling using the code NTSS [49].

In general, the strength of turbulent transport depends on normalized gradients lengths (e.g.$a/L_{T_i} = a\nabla T_i/T_i$) that provide free energy to the instabilities developing turbulence. One prominent instability is the ion temperature gradient (ITG) mode that causes radial transport of impurities via $\vec{E} \times \vec{B}$ drifts in presence of electrostatic fluctuations [9]. Possibly this mode is responsible for the anomalous impurity transport observed in W7-X since its drive, i.e. the a/L_{T_i} profile, resembles the shape of the experimental D_a profile. As plotted in figure 21, the two profiles have a similar shape for r_{eff}/a <0.6. Further outside, turbulence might become more and more suppressed

by the increasing density gradient and the increasing T_e/T_i ratio. As shown by [50], a critical gradient a/L_{crit} exists for temperature gradient driven modes which is defined by two competing terms. One term increases with the normalized electron density gradient length a/L_{n_e}, the other term decreases with the T_e/T_i ratio. In presence of low a/L_{n_e} values and high T_e/T_i ratios, ITG turbulence can thus exist. This is the case for the central plasma, as shown in figure 21. However, outside r_{eff}/a=0.6 a/L_{n_e} increases significantly and T_e/T_i becomes small. Thus, a/L_{crit} increases resulting in a reduced level of turbulence. This might explain the decrease of the experimental D_a profiles at r_{eff}/a >0.6.

In addition, the absence of a strong anomalous convection velocities ($v_a \approx 0$) agrees with the hypothesis of turbulent transport. From gyrokinetic theory, turbulent particle fluxes are ambipolar [51] such that the radial electric field, and hence the neo-classical transport should remain unchanged. Moreover, a direct turbulence-induced convection should be small, as reported recently by [8] (assuming quasi-linear theory).

7. SUMMARY

The impurity transport in H-plasmas of W7-X has been investigated in detail by analyzing the temporal behavior of Fe emission lines after a laser blow-off injection. Poor agreement is observed when comparing spectrometer measurements with STRAHL simulations that only consider neo-classical D_{nc} and v_{nc} profiles from DKES. In contrast, excellent agreement can be obtained when assuming additional anomalous D_a and v_a profiles in STRAHL, obtained using a least-squares fitting approach.

The resulting anomalous diffusion profile is well-defined through the time-delay of 9 different line emissions after the LBO injection, it increases towards the edge and exhibits values above 1.0 m^2/s. This is more than two orders of magnitude larger than the neo-classical expectation. Thanks to the optimization of W7-X with respect to neo-classical transport, the D_{nc} values are only in the range of 0.01 m^2/s. Also when modifying the kinetic profiles and E_r in DKES, the neo-classical diffusivities remain small which makes it robust and straightforward to conclude with anomalous impurity diffusion.

The conclusion whether there is an anomalous convection velocity is more difficult to draw. The fitted v_a profile is close to the neo-classical one and a fit with the assumption of v_a=0 yields an almost equally good representation of experimental data (also within the modeling uncertainties). However, it can be stated that the anomalous convection cannot be orders of magnitude larger than the neo-classical convection velocity. The observed impurity transport time (63 ms) restricts the minimum v/D value close to the edge and the v/D profile in the center is constrained by data from a soft X-ray imaging spectrometer (HR-XIS), measuring the Fe XXV emission profile at $r_{eff}/a < 0.6$.

The observation of a strong anomalous diffusion towards the edge and low anomalous convection velocities supports the hypothesis of turbulent impurity transport. Turbulent transport is dominated by ordinary Fickian diffusion and is expected at off-

axis positions due to its relation with normalized gradient lengths and the T_e/T_i ratio. Moreover, it is clear from a recent publication [48] that turbulent transport is present at W7-X since a significant contribution to the energy transport is observed.

With respect to the future exploitation of the stellarator concept, the observation of strong anomalous impurity transport is very promising. The anomalous transport could compensate for the inward-directed neo-classical convection velocity during core ion-root confinement conditions and might, thus, allow reactor-relevant long-pulse operation without accumulation.

8. ACKNOWLEDGMENTS

This work has been carried out within the framework of the EUROfusion Consortium and has received funding from the Euratom research and training programme 2014-2018 under Grant Agreement No. 633053. The views and opinions expressed herein do not necessarily reflect those of the European Commission.

[1] NEUHAUSER, J., Plasma Physics and Controlled Fusion **34** (1992) 2015.
[2] HELANDER, P. et al., Plasma Physics and Controlled Fusion **54** (2012) 124009.
[3] MAABERG, H. et al., Physics of Plasmas **7** (2000) 295.
[4] BURHENN, R. et al., Nuclear Fusion **49** (2009) 065005.
[5] NAKAMURA, Y. et al., Plasma Physics and Controlled Fusion **44** (2002) 2121.
[6] SUDO, S., Plasma Physics and Controlled Fusion **58** (2016) 043001.
[7] HELANDER, P. et al., Phys. Rev. Lett. **118** (2017) 155002.
[8] HELANDER, P. et al., Plasma Physics and Controlled Fusion **60** (2018) 084006.
[9] ANGIONI, C., Physics of Plasmas **22** (2015) 102501.
[10] DUX, R. et al., Plasma Physics and Controlled Fusion **45** (2003) 1815.
[11] BURHENN, R., B. J. B. R., Fusion Science and Technology **46** (2004) 115.
[12] TAMURA, N. et al., Plasma Physics and Controlled Fusion **45** (2003) 27.
[13] TAMURA, N. et al., Plasma Physics and Controlled Fusion **58** (2016) 114003.
[14] BEIDLER, C. et al., Fusion Technology **17** (1990) 148.
[15] KLINGER, T. et al., Plasma Physics and Controlled Fusion **59** (2017) 014018.
[16] HIRSHMAN, S. P. et al., The Physics of Fluids **29** (1986) 2951.
[17] BEHRINGER, K., PLASMA PHYSICS AND FUSION TECHNOLOGY **19** (1987) 57.
[18] LABOMBARD, B., Plasma Science and Fusion Center Research Report (2001) PSFC.
[19] GEIGER, J. et al., Plasma Physics and Controlled Fusion **57** (2015) 014004.
[20] RAHBARNIA, K. et al., Nuclear Fusion **58** (2018) 096010.
[21] BRUNNER, J., submitted to Journal of Instrumentation (2018).
[22] PASCH, E. et al., Review of Scientific Instruments **87** (2016) 11E729.
[23] BOZHENKOV, S. et al., Journal of Instrumentation **12** (2017) P10004.
[24] PABLANT, N. A. et al., Review of Scientific Instruments **83** (2012) 083506.
[25] WEGNER, T. et al., Review of Scientific Instruments **89** (2018) 073505.
[26] SATHEESWARAN, G. et al., Fusion Engineering and Design **123** (2017) 699 , Proceedings of the 29th Symposium on Fusion Technology (SOFT-29) Prague, Czech Republic, September 5-9, 2016.
[27] KOCSIS, G. et al., Fusion Engineering and Design **96-97** (2015) 808 , Proceedings of the 28th Symposium On Fusion Technology (SOFT-28).
[28] KRAMIDA, A. et al., NIST Atomic Spectra Database (ver. 5.5.6), National Institute of Standards and Technology, Gaithersburg, MD. (2018).

[29] BIEL, W. et al., Review of Scientific Instruments **75** (2004) 3268.
[30] THOMSEN, H. et al., Journal of Instrumentation **10** (2015) P10015.
[31] BERTSCHINGER, G. et al., Review of Scientific Instruments **75** (2004) 3727.
[32] LANGENBERG, A. et al., Review of Scientific Instruments **89** (2018) 10G101.
[33] MEISTER, H. et al., Review of Scientific Instruments **75** (2004) 4097.
[34] ZHOU, H. et al., Review of Scientific Instruments **81** (2010) 10D706.
[35] HINTON, F. L. et al., Rev. Mod. Phys. **48** (1976) 239.
[36] YOKOYAMA, M. et al., Nuclear Fusion **47** (2007) 1213.
[37] MAASSBERG, H. et al., Plasma Physics and Controlled Fusion **35** (1993) B319.
[38] STEPHEY, L. et al., Review of Scientific Instruments **87** (2016) 11D606.
[39] GONCHAROV, P. et al., Plasma Fusion Res. (2007) 1132.
[40] SINHA, P. et al., Nuclear Fusion **58** (2018) 016027.
[41] SUMMERS, H. P., The ADAS User Manual, version 2.6 http://www.adas.ac.uk (2004).
[42] PUETTERICH, T., to be submitted to Nuclear Fusion (2018).
[43] HIRSHMAN, S. et al., Computer Physics Communications **43** (1986) 143 .
[44] PUIATTI, M. E. et al., Physics of Plasmas **13** (2006) 042501.
[45] SERTOLI, M. et al., Plasma Physics and Controlled Fusion **53** (2011) 035024.
[46] ODSTRCIL, T. et al., Plasma Physics and Controlled Fusion **60** (2018) 014003.
[47] NEUHAUSER, J. et al., Journal of Nuclear Materials **121** (1984) 194 .
[48] FUCHERT, G., submitted to Nuclear Fusion (2018).
[49] TURKIN, Y. et al., Physics of Plasmas **18** (2011) 022505.
[50] JENKO, F. et al., Physics of Plasmas **8** (2001) 4096.
[51] HELANDER, P., Reports on Progress in Physics **77** (2014) 087001.